Supplementary Information (SI) for Journal of Materials Chemistry A.

Supporting Information

Orchestrating Dual-Interface Stabilization via a Threefold Mechanistic Synergy of Aluminum Dihydrogen Phosphate for Ultrastable Aqueous Zinc-Ion Batteries

Ming Hao[1], Jinwei Zhou[2] , Rongyu Deng[3], Chuanli Qin[1,] Feixiang Wu[2,]**

[1] School of Chemistry and Materials Science, International Joint Research Center for Catalytic Technology, Heilongjiang University, Harbin 150080, People's Republic of China

[2] National Engineering Research Center of Advanced Energy Storage Materials, School of Metallurgy and Environment, Central South University, Changsha 410083, PR China

[3] Department of Material Science and Engineering, College of Design and Engineering, National University of Singapore, 9 Engineering Drive 1, Singapore, Singapore 117575, Singapore

Methods

Electrolyte preparation

The baseline electrolyte (denoted as BE) consisted of 2 M $ZnSO_4$ in deionized (DI) water. For Zn||MnO_2 full cell assembly, 0.1 M $MnSO_4$ was added to the electrolyte to suppress the dissolution of manganese from the cathode via the common-ion effect. The modified electrolyte (denoted as ADP) was prepared by dissolving 0.02 M $Al(H_2PO_4)_3$ into the baseline electrolyte under continuous stirring until a homogeneous solution was obtained. All chemicals, including $ZnSO_4 \cdot 7H_2O$ and $Al(H_2PO_4)_3$, were purchased from Aladdin Reagent (Shanghai) Co., Ltd. and used as received without further purification.

Synthesis of cathode materials

The cathode active materials were synthesized via a hydrothermal method. Briefly, 0.1 g of carbon nanotubes (CNTs) was dispersed in 60 mL of DI water via ultrasonication. Subsequently, 0.486 g of $KMnO_4$ was added and stirred until completely dissolved. Separately, 1.135 g $Mn(CH_3COO)_2 \cdot 4H_2O$ was dissolved in 20 mL DI-water and poured into the suspension. The mixture was stirred for 10 min and ultrasonicated for another 60 min to ensure uniformity. The precursor solution was then transferred into a Teflon-lined stainless steel autoclave and maintained at 120 °C for 12 h. The resulting precipitate was collected, washed with DI water and ethanol, and finally lyophilized (freeze-dried) for 72 h to obtain the final product.

Materials characterization

X-ray diffraction (XRD) patterns were recorded on a PANalytical Empyrean 2 diffractometer using Cu Kα radiation. The morphology and elemental distribution were characterized by scanning electron microscopy (SEM, TESCAN MIRA LMS) equipped with an energy-dispersive X-ray spectroscopy (EDS) detector. Fourier transform infrared (FTIR) spectra of the electrolytes were acquired using a Thermo Fisher Scientific Nicolet iS10 spectrometer. Raman spectra were collected at room temperature using a confocal Raman spectrometer (Horiba LabRAM HR800, France) with a 532 nm excitation laser. X-ray photoelectron spectroscopy (XPS) measurements were performed on a PHI 5000 VersaProbe II spectrometer utilizing a monochromatic Al Kα X-ray source.

Electrochemical measurement

The cathode slurry was prepared by dispersing α-MnO_2, Super P conductive carbon, and polyvinylidene fluoride (PVDF) binder in N-methyl-2-pyrrolidone (NMP) at a mass ratio of 7:2:1. The mixture was stirred for 12 h to ensure homogeneity and then cast onto a stainless steel foil current collector. After drying in a vacuum oven at 80 °C overnight, the electrode was punched into discs with a diameter of 1.0 cm. The mass loading of the active material (α-MnO_2) was controlled within 0.8–1.2 mg cm^{-2}, and the specific capacity was calculated based on this mass. For the anode, zinc metal foils (thickness: 0.1 mm) were punched into 1.2 cm diameter discs. CR2032 coin-type cells were assembled in an air atmosphere using Whatman glass fiber membranes (GF/D, 1.9 cm in diameter) as separators. Battery performance was evaluated using a LAND CT2001A battery testing system (Wuhan Land Electronic Co. Ltd., China) in a thermostatic chamber at 25 °C. The cycling stability of the Zn anode was assessed in symmetric Zn||Zn cells. The Coulombic efficiency (CE) of Zn plating/stripping was determined using asymmetric Zn||Cu cells, cycled between 0 and 0.5 V (vs. Zn^{2+}/Zn). For full cells (Zn||MnO_2), galvanostatic charge-discharge (GCD) tests were conducted within a voltage window of 0.8–1.8 V at various current densities ranging from 0.1 to 5 A g^{-1}. Cyclic voltammetry (CV), electrochemical impedance spectroscopy (EIS), linear sweep voltammetry (LSV), and chronoamperometry (CA) were performed on a Gamry electrochemical workstation. Different CV measurements were conducted under different cell configurations and testing conditions depending on their specific purposes. For Zn nucleation analysis (Fig. 3b), CV was performed using Zn||Cu asymmetric cells at a scan rate of 10 mV s^{-1}. For the general electrochemical behavior of full cells (Fig. 6a and Fig. S25), CV was recorded using Zn||MnO_2 full cells at 0.1 mV s^{-1} within a voltage range of 0.8-1.8 V. For the scan-rate-dependent diffusion-kinetics analysis (Fig. 6b and Fig. S26), CV was conducted using Zn||MnO_2 full cells at scan rates of 0.2, 0.4, 0.6, 0.8, and 1.0 mV s^{-1} within 0.8-1.8 V. EIS measurements were carried out over a frequency range of 100 kHz to 0.01 Hz with a sinusoidal amplitude of 10 mV. The electrochemical stability window was evaluated via LSV using a two-electrode configuration (stainless steel working electrode vs. Zn counter/reference electrode) at a scan rate of 1 mV s^{-1}. Nucleation overpotentials were analyzed via CA tests at a constant overpotential of -150 mV. The Zn^{2+} transference number ($t_{Zn}{}^{2+}$) was determined using the Bruce-Vincent method, which involves polarizing a Zn||Zn symmetric cell at a constant voltage ($\triangle V$ = 10 mV) for 3600 s while recording the initial and steady-state currents (I_0 and I_s), combined with EIS measurements before and after polarization (R_0 and R_s). The transference number is calculated as:

$$t_{Zn^{2+}} = \frac{I_s(\Delta V - R_0 I_0)}{I_0(\Delta V - R_s I_s)} \#(eq.S1)$$

The apparent ion diffusion coefficients were estimated from the cyclic voltammetry (CV) curves measured at various scan rates (v) ranging from 0.2 to 1.0 mV s^{-1}. The relationship between the peak current (i_p) and the square root of the scan rate ($v^{1/2}$) was analyzed using the Randles-Sevcik equation. It should be noted that the obtained values represent apparent diffusion-related parameters derived from the Zn||MnO_2 full-cell response, rather than intrinsic solid-state Zn^{2+} diffusion coefficients:

$$i_p = 2.69 \times 10^5 \cdot n^{3/2} \cdot A \cdot D^{1/2} \cdot C \cdot v^{1/2} \#(eq.S2)$$

where i_p represents the peak current (A), n is the number of electrons transferred (n = 2 for Zn^{2+}), A is the active surface area of the electrode (cm^2), D is the diffusion coefficient (cm^2 s^{-1}), C corresponds to the molar concentration of zinc ions (mol cm^{-3}), and v denotes the scan rate (V s^{-1}).

By plotting ip versus $v^{1/2}$, the apparent diffusion coefficient can be estimated from the slope (k) of the linear fitting curve using the following equation:

$$D = \left(\frac{k}{2.69 \times 10^5 \cdot n^{3/2} \cdot A \cdot C} \right)^2 \#(eq.S3)$$

Galvanostatic charge/discharge tests of batteries were recorded using a LAND-CT3001A battery testing system. Electrochemical impedance spectroscopy (EIS) for ionic-conductivity measurements was performed on a Gamry Interface-1000E electrochemical workstation over a frequency range from 1 MHz to 0.1 Hz with an amplitude voltage of 10 mV. Stainless-steel symmetric cells (SS||SS) assembled with glass fiber separators soaked with the corresponding liquid electrolytes were used to measure the impedance resistance (R) and calculate the ionic conductivities of the liquid electrolytes from −20 to 60 °C. The ionic conductivity (σ) was calculated according to the following equation:

$$\sigma = \frac{l}{SR} \#(eq.S4)$$

where l (cm) is the thickness of the electrolyte-soaked separator, S (cm^2) is the effective contact area with the stainless-steel electrode, and R (Ω) is the bulk resistance obtained from EIS. In this work, l and S were 0.15 cm and 0.5024 cm^2, respectively.

The activation energy (E_a) for ion transport within the electrolytes is evaluated based on the empirical Arrhenius equation:

$$\sigma = \mathrm{A}e^{-\frac{E_a}{RT}} \#(eq.S5)$$

where σ is the ionic conductivity, A is the pre-exponential factor, T is the absolute thermodynamic temperature (K), and R is the universal gas constant (8.314 J mol^{-1} K^{-1}). Because the temperature T acts in the exponential term, a minor temperature variation induces a pronounced change in the conductivity. Taking the natural logarithm (ln) of both sides yields:

$$ln\,\sigma = -\frac{E_a}{RT} + ln\,A \#(eq.S6)$$

To correlate with the linear fitting presented in Figure S28, the natural logarithm is converted to the common logarithm (base 10, denoted as log):

$$log\,\sigma = -\frac{E_a}{2.303RT} + log\,A \#(eq.S7)$$

Given that the x-axis in Figure S28 is expressed as 1000/T, the equation can be further rearranged into the following linear form:

$$log\,\sigma = \left(-\frac{E_a}{2303R}\right)\left(\frac{1000}{T}\right) + log\,A \#(eq.S8)$$

Assuming E_a is relatively independent of temperature within the tested range, plotting $\log\sigma$ against $1000/T$ yields a straight line. Consequently, the activation energy can be estimated from the slope of this linear fit:

$$E_a = -2303R \times Slope \#(eq. S9)$$

Computational Methods

DFT Calculations

First-principles calculations were conducted based on the density functional theory (DFT) framework. The electronic exchange-correlation interaction was described by the generalized gradient approximation (GGA) with the Perdew-Burke-Ernzerhof (PBE) functional.[1] To accurately describe weak intermolecular interactions, the Tkatchenko-Scheffler (TS) dispersion correction scheme was employed to account for van der Waals forces. A double numerical plus polarization (DNP) basis set was adopted for high-precision orbital expansion. Geometry optimizations were performed with strict convergence criteria: 1.0 × 10^{-5} Ha for energy change, 0.002 Ha Å^{-1} for maximum force, and 0.005 Å for displacement. The self-consistent field (SCF) density convergence threshold was set to 1.0 × 10^{-6}. Interaction configurations were initially screened via Monte Carlo simulations and subsequently fully relaxed. Based on the equilibrium structures, the frontier molecular orbitals (HOMO/LUMO), electrostatic potential (ESP), and charge density difference were computed to analyze the intermolecular interactions. The binding energy (E_b) was defined as:[2]

$$E_b = E_{pair} - E_{solute} - E_{solvent} \#(eq. S10)$$

Where E_{pair} denotes the total energy of the optimized complex, while E_{solute}, and $E_{solvent}$ refer to the energies of the isolated species.

Adsorption calculations for H_2O and $H_2PO_4^-$ anion on various Zn crystal facets were performed using density functional theory (DFT) as implemented in the CASTEP module of Materials Studio. The projector augmented wave (PAW) method combined with the Perdew-Burke-Ernzerhof (PBE) exchange-correlation functional was employed to describe the ion-electron interactions. A plane-wave basis set with a cutoff energy of 500 eV was utilized. The convergence criterion for the electronic self-consistent field (SCF) iteration was set to 1.0 × 10^{-6} eV. The Zn (002), (100), and

(101) electrode surfaces were modeled using supercells with dimensions of 5 × 5 , 4 × 3, and 3 × 4, respectively. Each slab model consisted of at least four atomic layers. To simulate the bulk properties while allowing for surface reconstruction, the bottom two atomic layers were fixed, while the top two layers and the adsorbates were allowed to fully relax. To eliminate spurious interactions between periodic images, a vacuum layer of 15 Å was applied along the z-direction. All structures were fully relaxed until the force on each atom converged to less than 0.05 eV/Å. The adsorption energy (E_{ads}) for Zn^{2+}, Al^{3+}, H_2O and $H_2PO_4^-$ was calculated using the following equation:

$$E_{ads} = E_{total} - (E_{slab} + E_{adsorbate}) \#(eq. S11)$$

Where E_{total},$E_{slab}$and $E_{adsorbate}$denote the total energies of the adsorbate-substrate system, the pristine Zn slab, and the isolated adsorbate molecule/ion, respectively.

Molecular dynamics simulations

To ensure the accuracy of intermolecular interactions, a combined Quantum Mechanics (QM) and Molecular Dynamics (MD) approach was adopted. First, the geometries of all electrolyte components, including H_2O, SO_4^{2-}, Zn^{2+}, Al^{3+}, and $H_2PO_4^-$, were optimized using density functional theory (DFT) via the DMol3 module in Materials Studio. The calculations employed the GGA-PBE functional with a double numerical plus polarization (DNP) basis set. The DFT-D method developed by Grimme was applied to account for van der Waals interactions. The convergence criteria for energy change, maximum force, and maximum displacement were set to 1.0×10^{-5} Ha, 0.002 Ha $Å^{-1}$, and 0.005Å, respectively. Crucially, the atomic partial charges were derived from the Electrostatic Potential (ESP) fitting method based on the optimized electron density, providing a rigorous physical description of the electrostatic environment.

Subsequently, Molecular dynamics (MD) simulations were performed using GROMACS (version 2023.2).[3] All molecules were first geometry-optimized with Gaussian 16.[4] The simulation boxes were built with Packmol.[5] The baseline electrolyte system (System A) consisted of 100 Zn^{2+}, 100 SO_4^{2-}, and 2670 H_2O molecules. The ADP-containing electrolyte (System B) was composed of 100 Zn^{2+}, 100 SO_4^{2-}, 10 Al^{3+}, 30 $H_2PO_4^-$, and 2670 H_2O molecules. Interactions among the molecules and ions were described using the General AMBER Force Field 2 (GAFF2) and SPC/E water model.[6,7] RESP charge obtained from Multiwfn[8] was applied in the calculations. To account for polarization effects, the charges of the cations and anions were scaled by a factor of 0.8. After the energy minimization, the system was equilibrated in the NPT ensemble at 373 K for 500 ps, and then further equilibrated at 298.15 K for 2 ns. After that, the production run was carried out in the NVT ensemble at 298.15 K with the time step of 1 fs. The temperature of the system was controlled by a V-rescale thermostat (τ_T = 1 ps). The long-range electrostatic interactions were executed utilizing the Particle Mesh Ewald (PME) method. A cutoff length of 1.2 nm was utilized for real-space electrostatic interaction. After 5 ns of simulation, the RDF and CN were analyzed by the toolkits of GROMACS.

Finite Element Modeling (FEM)

Finite element simulations were performed using COMSOL Multiphysics 6.3 to elucidate the spatial distributions of electric-field intensity, current density, and Zn^{2+} concentration at the anode/electrolyte interface. The Tertiary Current Distribution, Nernst-Planck, and Phase Field modules were coupled to capture the electrochemical deposition behavior. Ion transport within the electrolyte was governed by the Nernst-Planck equation, which accounts for both diffusion and electromigration.

The geometric model represented a simplified rough Zn anode surface containing five equidistant protrusions to mimic initial dendrite nuclei or surface roughness. The simulation domain consisted of two parallel electrodes with a length of 6 μm and an interelectrode distance of 5 μm. For the boundary conditions, the counter electrode was grounded at 0 V, while the Zn electrode was assigned the polarization potential derived from the corresponding experimental cell tests. The initial Zn^{2+} concentration in the electrolyte was set to 2 M, corresponding to 2000 mol m^{-3}. The Zn^{2+} diffusion coefficients were set to 5.29×10^{-17} m^2 s^{-1} for the bare $ZnSO_4$ electrolyte and 1.96×10^{-14} m^2 s^{-1} for the ADP-containing electrolyte. The exchange current density and system temperature were set to 10 mA cm^{-2} and 298 K, respectively. For direct comparison, the same geometric model, electrode spacing, initial Zn^{2+} concentration, applied potential condition, and color scale were used for each paired simulation of the bare $ZnSO_4$ and ADP-containing electrolytes; only electrolyte-dependent transport parameters, such as the Zn^{2+} diffusion coefficient, were changed according to the experimentally derived values.

The mass transport of Zn^{2+} driven by the concentration gradient follows Fick's first law:[9]

$$J=-D\nabla_{C} \#(eq.S12)$$

where J is the diffusion flux (mol m^{-2} s^{-1}), D is the diffusion coefficient (m^2 s^{-1}), and ∇c is the concentration gradient (mol m^{-4}). Considering the electric field effect, the total ion transport is described by the Nernst-Planck equation, which relates the diffusion coefficient to electric mobility:

$$N_i=-D_i\nabla c_i-z_iu_mFc_i\nabla\phi \#(eq.S13)$$

Where N_i is the total flux vector (mol/(m^2·s)), c_i is the ion concentration (mol/m^3), z_i is the valence of the ionic species (+2 for Zn^{2+}), u_m is the mobility of the charged species, F is Faraday's constant (96485 C mol^{-1}), ϕ is the electrolyte potential.

The electrochemical reaction kinetics at the electrode interface are described by the Butler-Volmer equation, which governs the local current density distribution:

$$i_{loc}=i_0\left[exp\left(\frac{\alpha_aF\eta}{RT}\right)-exp\left(-\frac{\alpha_cF\eta}{RT}\right)\right] \#(eq.S14)$$

where i_{loc} represents the local current density, i_0 is the exchange current density, η is the overpotential ($\eta=\phi_s-\phi_l-E_{eq}$), where ϕ_s is the solid phase potential and ϕ_l is the electrolyte potential. α_a and α_c are the anodic and cathodic charge transfer coefficients, respectively, R is the ideal gas constant, and T is the absolute temperature.

Supplementary Figures

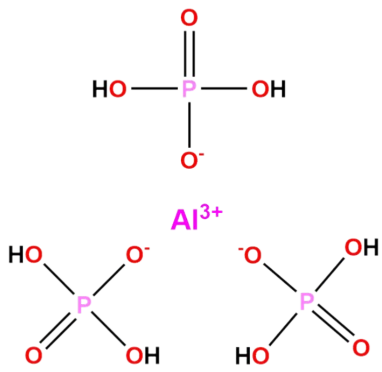

Fig. S1 Schematic of the molecular formula of ADP.

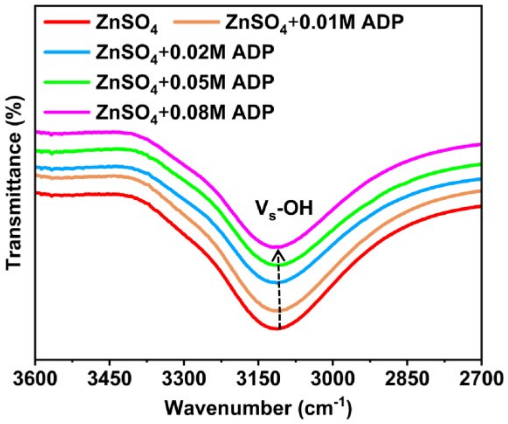

Fig. S2 FTIR spectra in the range of 3600 ~ 2700 cm^{-1} of $ZnSO_4$ electrolytes with different ADP contents.

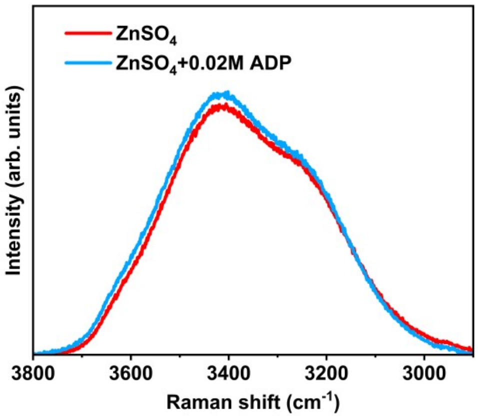

Fig. S3 Comparison of Raman spectra of different electrolytes.

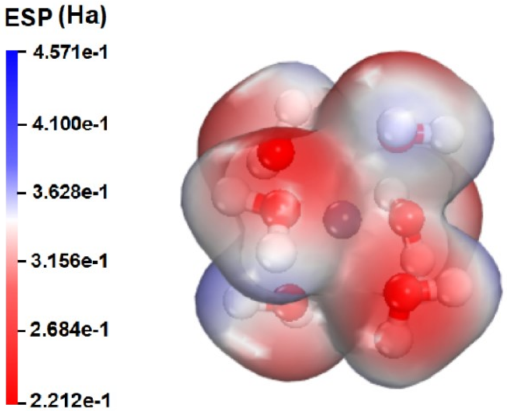

Fig. S4 Electrostatic potential mapping of the original Zn^{2+}-$6H_2O$ solvation structure.

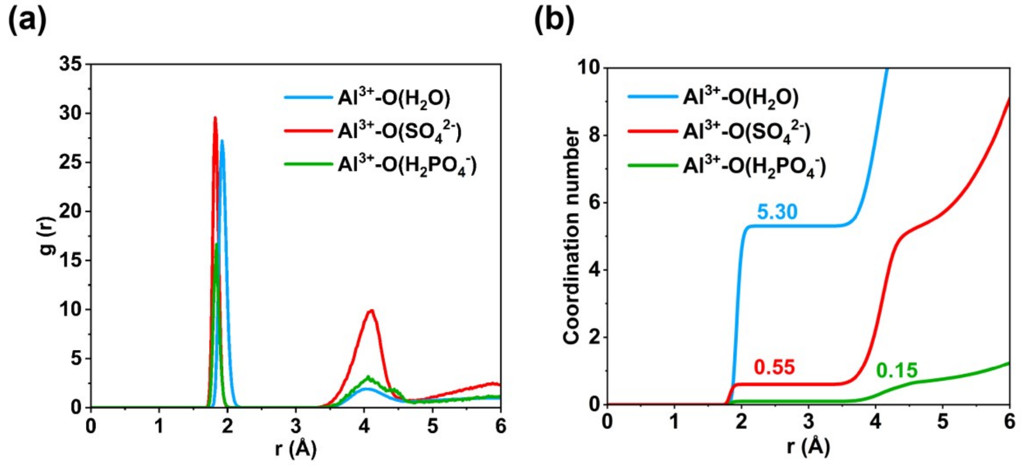

Fig. S5 Solvation structure of Al^{3+} in the ADP-containing electrolyte derived from molecular dynamics (MD) simulations. (a) Radial distribution function (RDF, g(r)) profiles and (b) the corresponding cumulative coordination numbers for the Al^{3+}-O(H_2O), Al^{3+}-O($H_2PO_4^-$), and Al^{3+}-O(SO_4^{2-}) pairs.

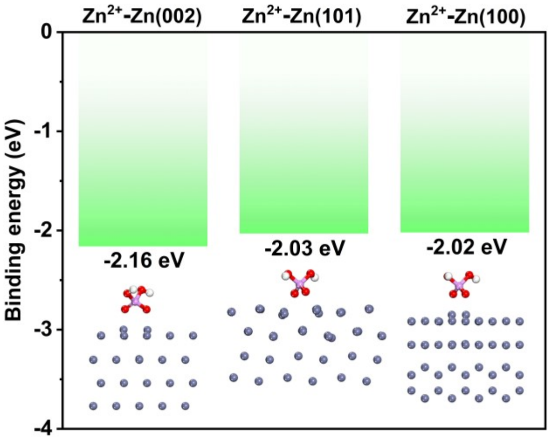

Fig. S6 Calculated binding energies and corresponding optimized adsorption configurations of $H_2PO_4^-$ anions on the Zn (002), (101), and (100) crystal planes.

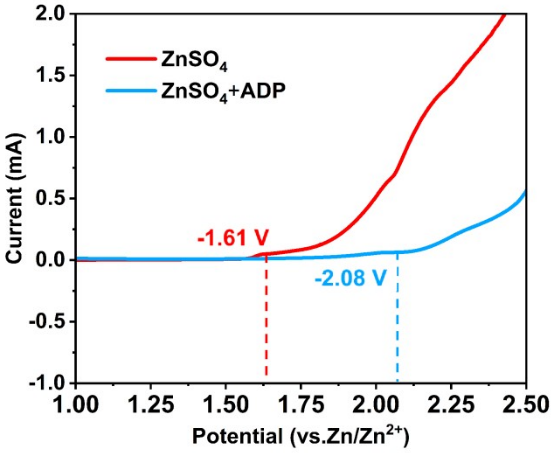

Fig. S7 Linear sweep voltammetry depicting the OER with varying electrolytes at a scan rate of 1 mV s^{-1}.

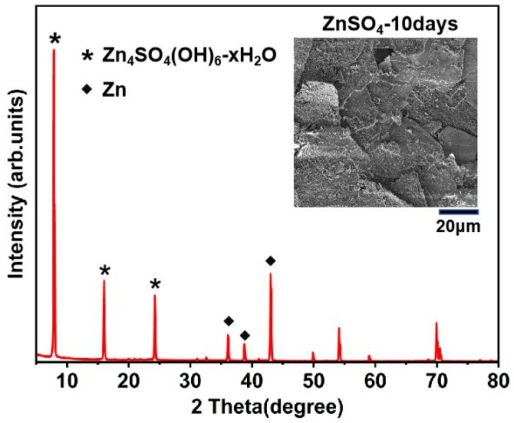

Fig. S8 X-ray diffraction pattern of zinc foil immersed in $ZnSO_4$ electrolyte for 10 days (illustration shows corresponding SEM image).

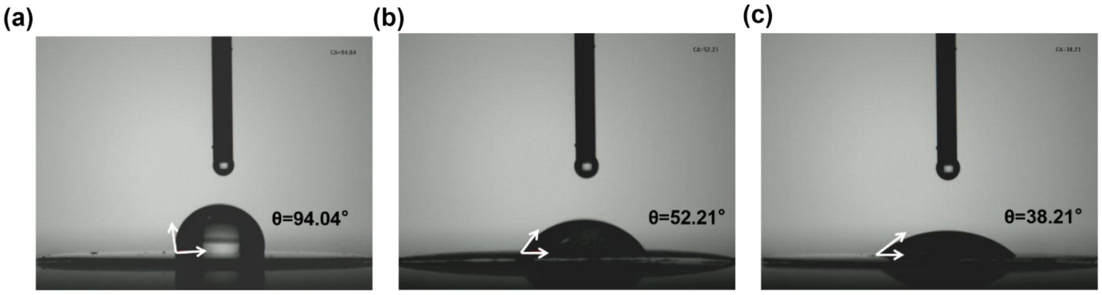

Zn-$ZnSO_4$ - 0 days

$ZnSO_4$ - 10 days

$ZnSO_4$ -ADP -10 days

Fig. S9 Contact angle images of distilled water on the surfaces of (a) pristine bare Zn foil, (b) Zn foil after 10 days of immersion in the baseline $ZnSO_4$ electrolyte, and (c) Zn foil after 10 days of immersion in the ADP-containing electrolyte.

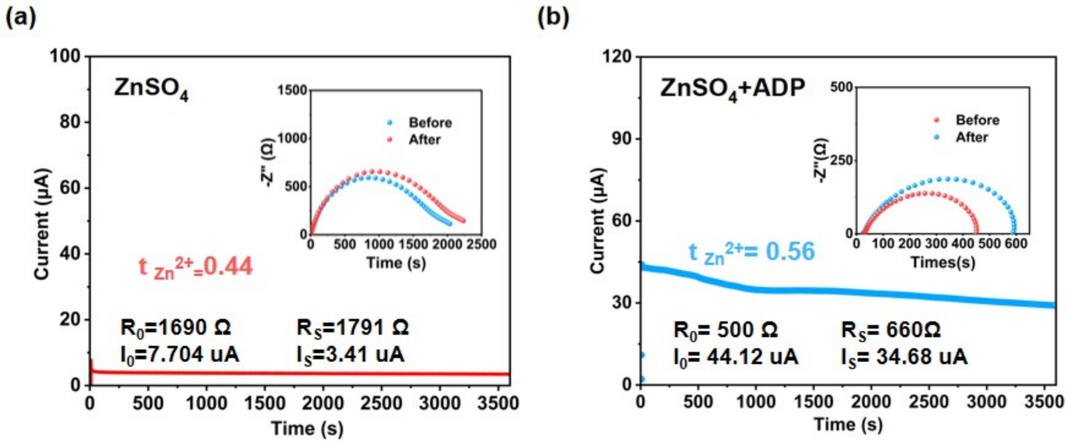

Fig. S10 Zn^{2+} transference number characterizations for (a) $ZnSO_4$ and (b) $ZnSO_4$-ADP electrolytes.

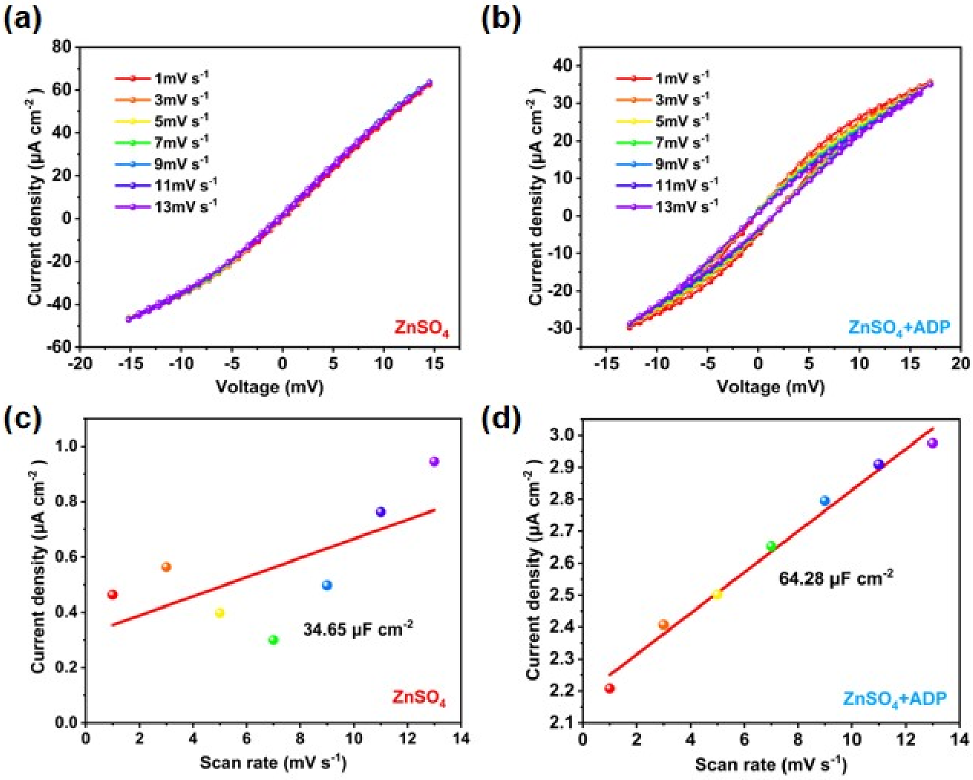

Fig. S11 (a) Cyclic voltammetry curves of symmetric cells using a $ZnSO_4$ electrolyte at different scan rates. (b) Cyclic voltammetry curves of symmetric cells containing ADP at different scan rates. (c) (d) Electrode double layer measurements for different electrolytes.

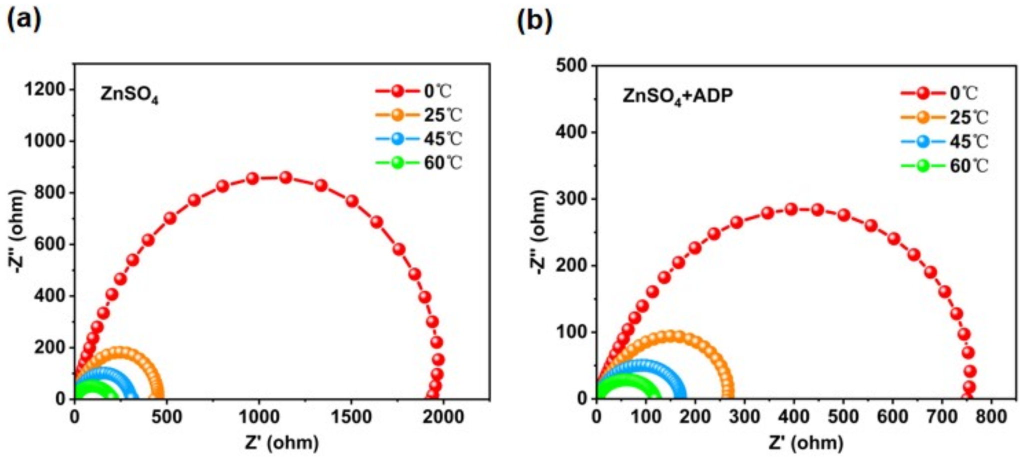

Fig. S12 EIS characterisation of symmetrical zinc batteries containing (a) $ZnSO_4$ and (b) $ZnSO_4$-ADP electrolytes at different temperatures.

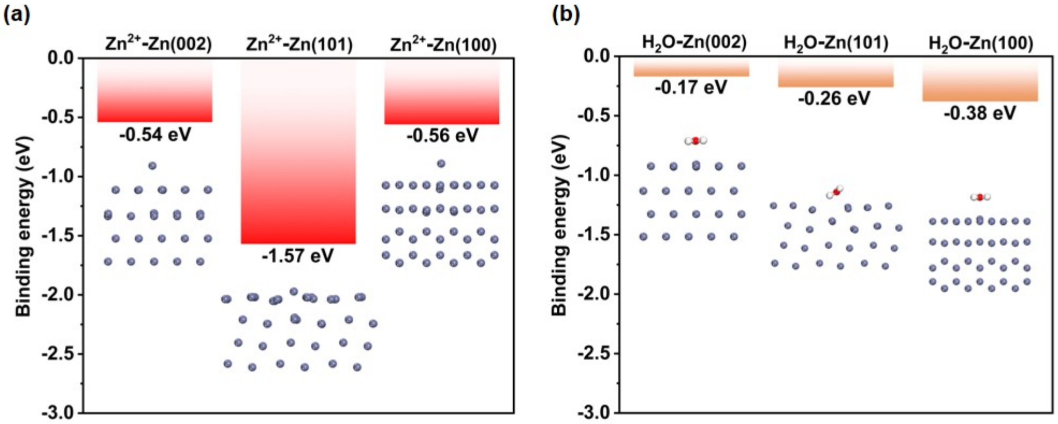

Fig. S13 Calculated adsorption energies and corresponding optimized configurations of (a) Zn^{2+} ions and (b) H_2O molecules on the Zn (002), (101), and (100) crystal planes.

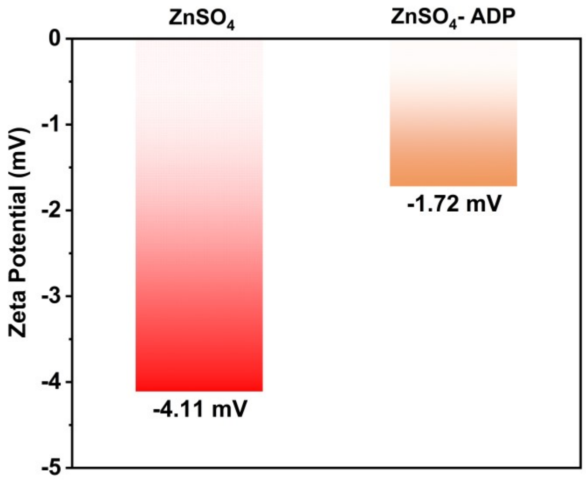

Fig. S14 Statistical Zeta Potential of Zinc Deposits in ZnSO$_4$ and ZnSO$_4$-ADP Electrolytes.

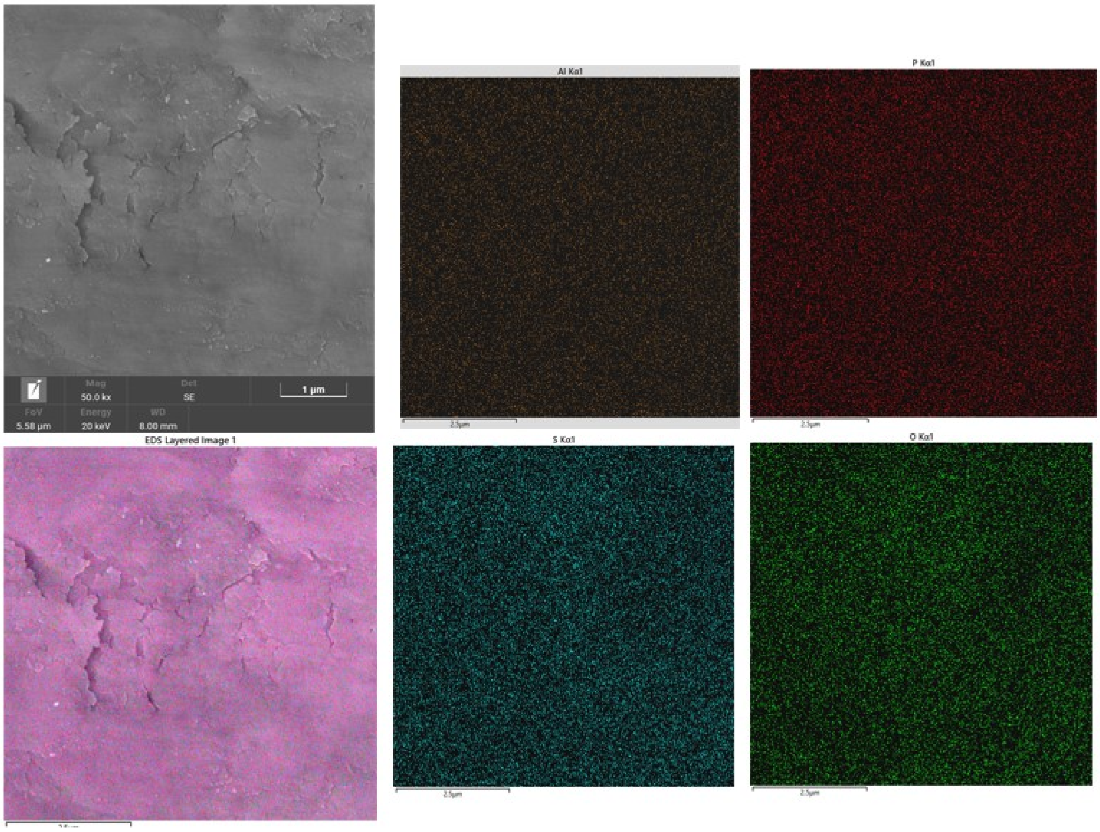

Fig. S15 EDX mapping of the cycled Zn electrode in the ADP-containing electrolyte.

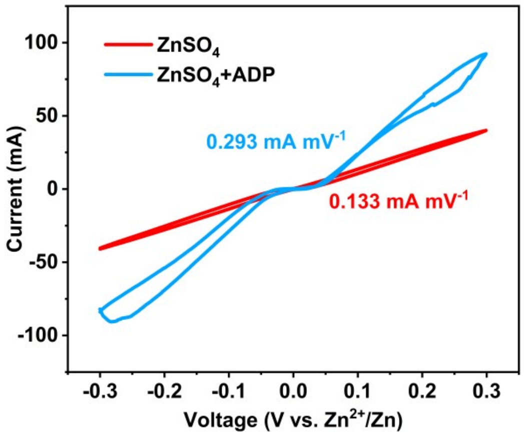

Fig. S16 CV curves of Zn||Zn symmetrical cells in $ZnSO_4$ and $ZnSO_4$ + ADP electrolytes at 1 mV s^{-1}.

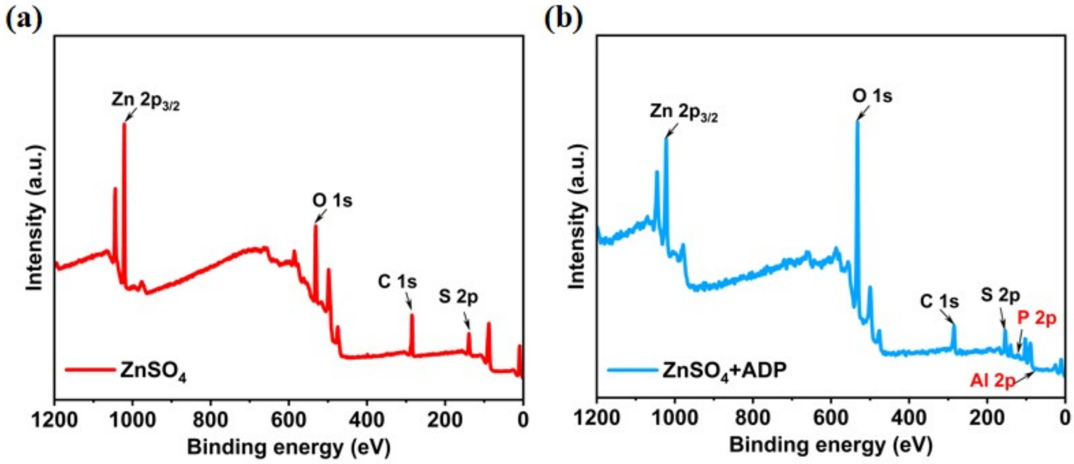

Fig. S17 XPS spectra of zinc after 1000 cycles in a Zn//Zn symmetric cell with the following electrolytes: (a) $ZnSO_4$ and (b) $ZnSO_4$ + ADP.

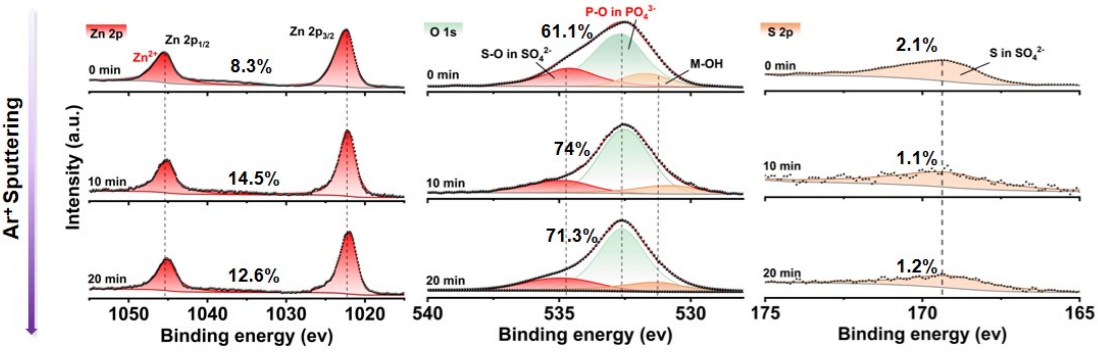

Fig. S18 Depth-resolved high-resolution XPS spectra of Zn 2p, O 1s, and S 2p regions for the Zn anode after cycling.

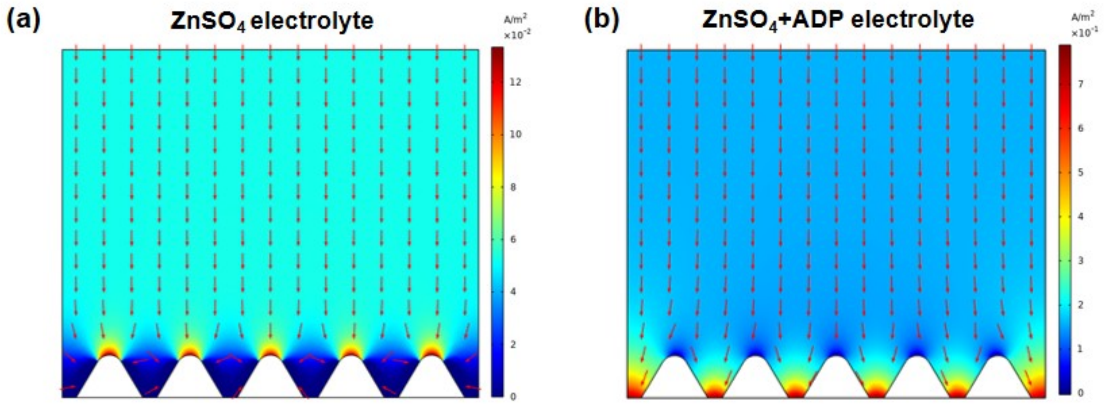

Fig. S19 FEM-simulated current-density distributions on rough Zn anodes in (a) bare $ZnSO_4$ and (b) ADP-containing electrolytes. The same color scale is used in (a,b) for direct comparison.

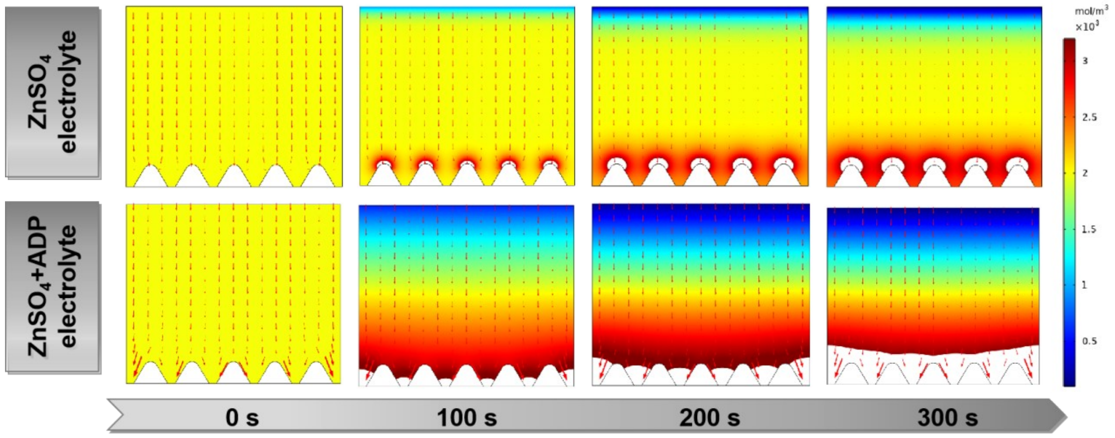

Fig. S20 FEM-simulated dynamic evolution of Zn^{2+} concentration fields in the bare $ZnSO_4$ and ADP-containing electrolytes from 0 to 300 s. The color bars represent Zn^{2+} concentration, and the same color scale is used for the corresponding time points to enable direct comparison between the two electrolytes.

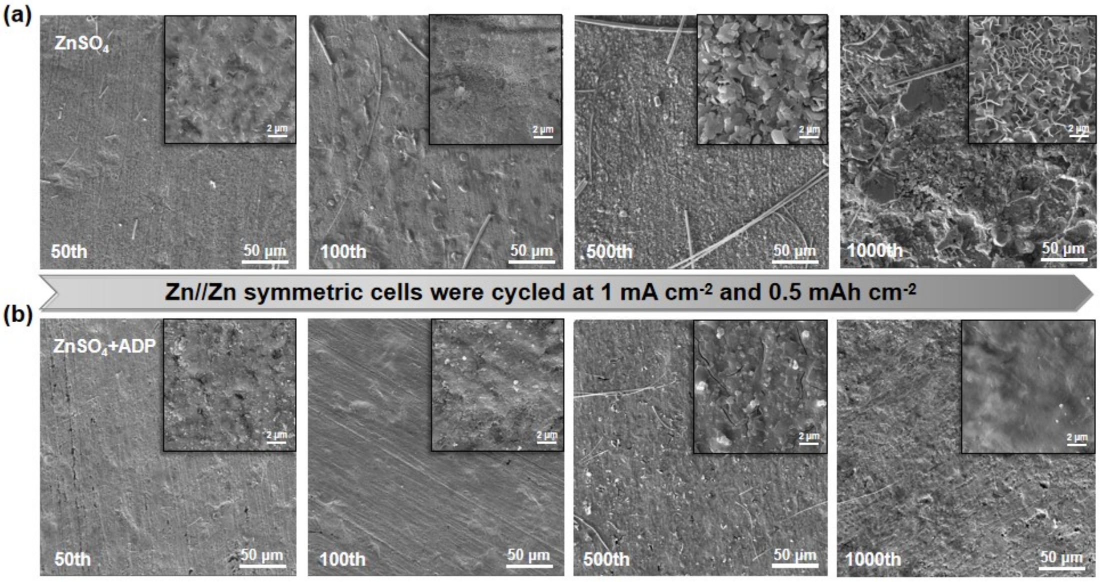

Fig. S21 Ex situ surface scanning electron microscopy (SEM) images of the zinc electrodes retrieved from Zn//Zn symmetric cells after different cycles (50th, 100th, 500th, and 1000th) at 1 mA cm^{-2} and 0.5 mAh cm^{-2} in (a) bare ZnSO$_4$ and (b) ADP-containing electrolytes.

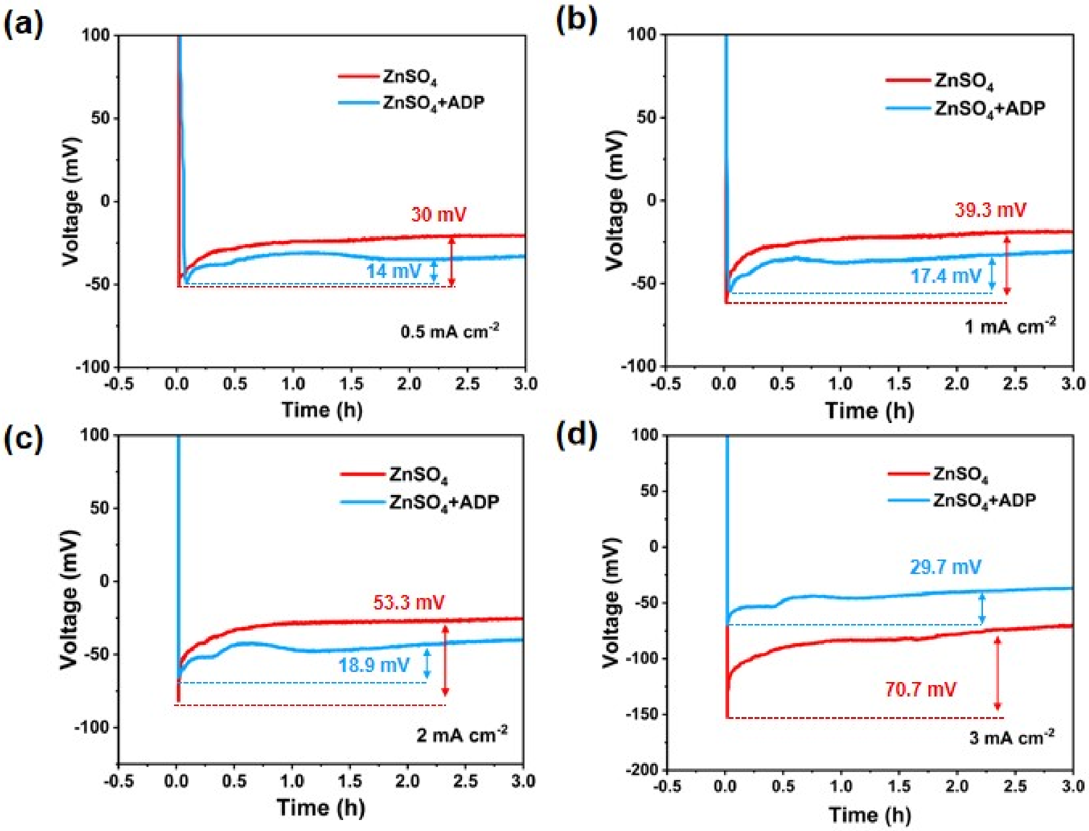

Fig. S22 Galvanostatic Zn deposition on Cu in different electrolytes at current densities of (a) 0.5, (b) 1.0, (c) 2.0, and (d) 3.0 mA cm^{-2}.

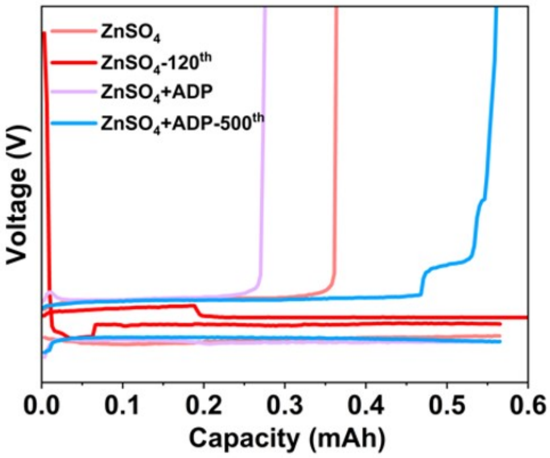

Fig. S23 Charge-discharge voltage profiles of the Zn||Cu asymmetric cells at selected cycles in the bare $ZnSO_4$ and ADP-containing electrolytes at 1 mA cm^{-2} with a capacity of 0.5 mAh cm^{-2}.

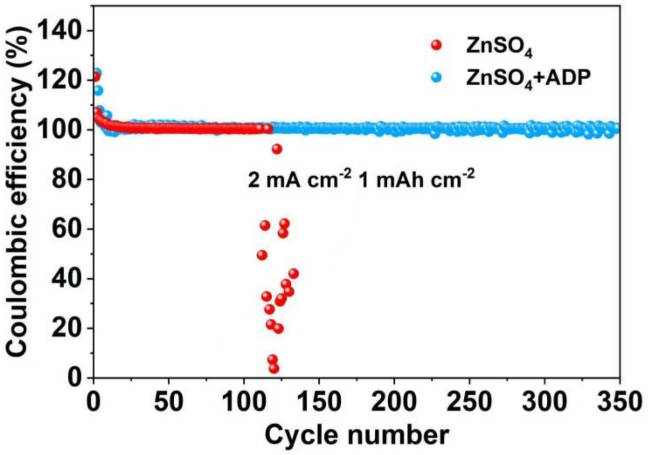

Fig. S24 Coulombic efficiency of Zn||Cu cells with different electrolytes at 2 mA cm^{-2}, 1 mAh cm^{-2} discharge capacity, 0.5 mV charge cut-off voltage, and temperature of 25 ℃.

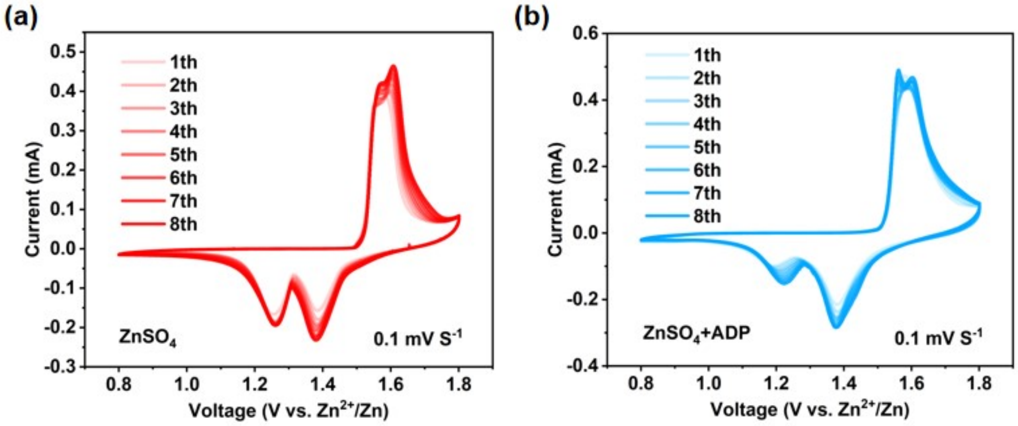

Fig. S25 Successive CV profiles of the Zn||MnO_2 full cells over the first 8 cycles in (a) bare $ZnSO_4$ and (b) ADP-containing electrolytes recorded at 0.1 mV s^{-1} within 0.8-1.8 V.

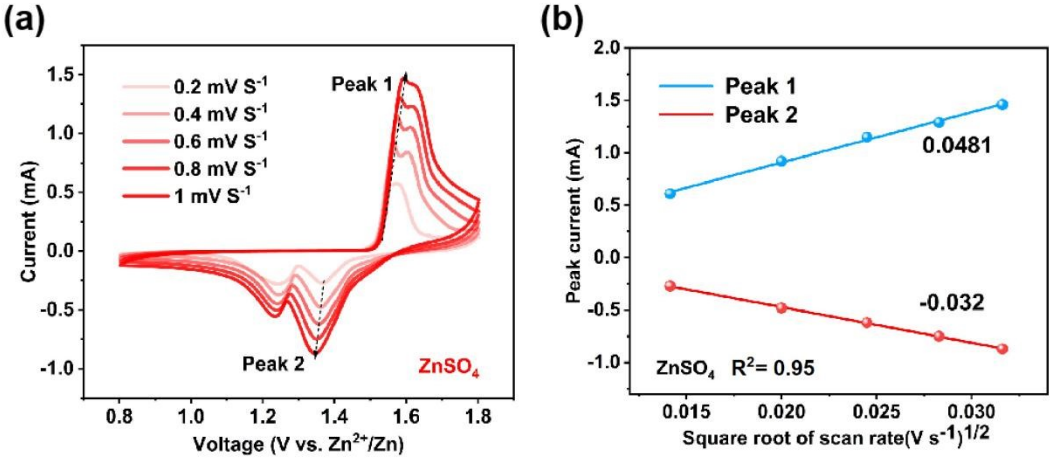

Fig. S26 Kinetic analysis of the bare $ZnSO_4$ electrolyte in Zn||MnO_2 full cells. (a) CV curves recorded at scan rates of 0.2, 0.4, 0.6, 0.8, and 1.0 mV s^{-1} within 0.8-1.8 V. (b) Corresponding linear fitting of peak currents versus the square root of scan rates ($v^{1/2}$), with the R^2 values included in the fitting plots.

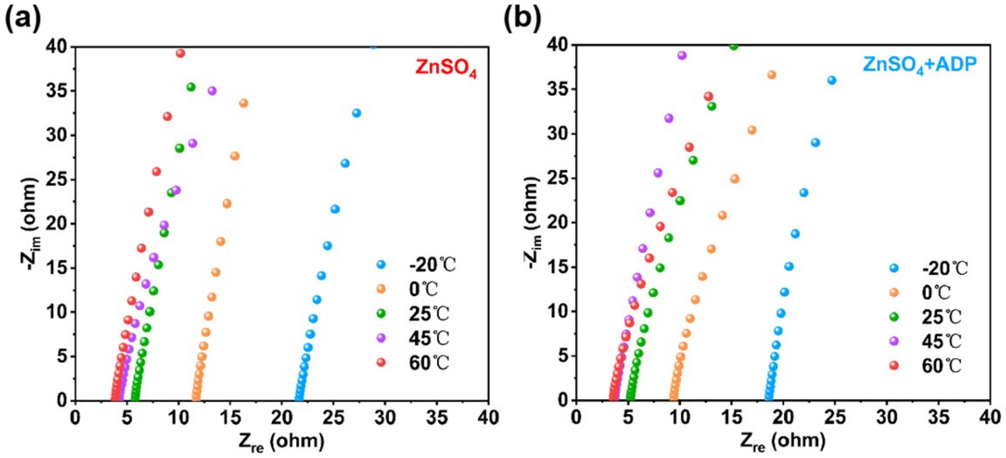

Fig. S27 Nyquist plots of stainless-steel symmetric cells (SS||SS) containing (a) bare $ZnSO_4$ and (b) ADP-containing liquid electrolytes measured at various temperatures from -20 to 60 ˚C.

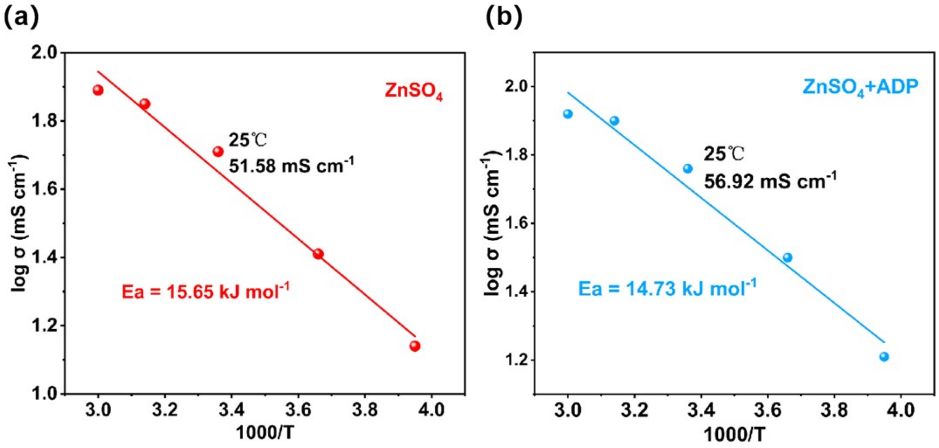

Fig. S28 Temperature-dependent ionic conductivity of the bare $ZnSO_4$ and ADP-containing liquid electrolytes within a temperature range from -20 to 60 ˚C. The solid lines represent fitting results based on the Arrhenius model.

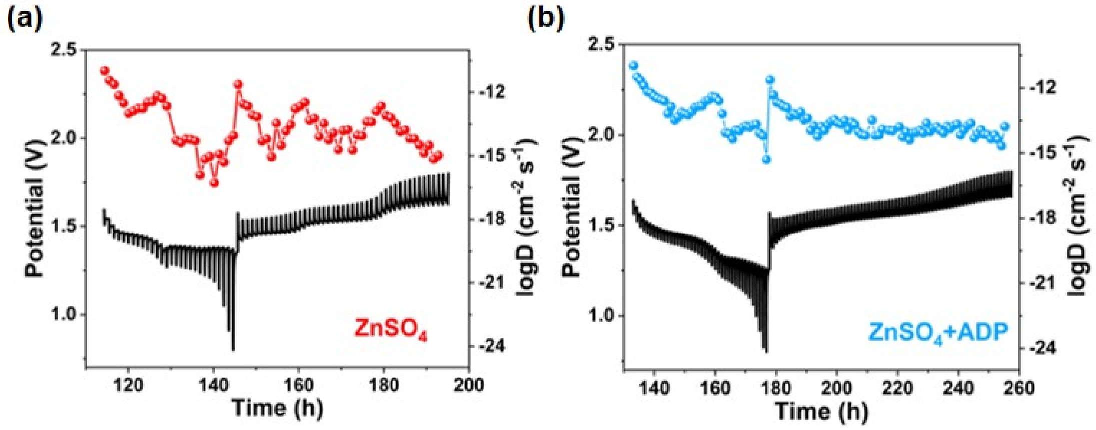

Fig. S29 Charge–discharge GITT profiles at 0.2 A g^{-1} between 0.8 and 1.8 V in the 4th cycle and corresponding apparent diffusion coefficients of Zn||MnO$_2$ full cells using (a) ZnSO$_4$ and (b) ZnSO$_4$ + ADP electrolytes.

Fig. S30 Electrolyte storage test. Digital photographs of electrolytes after resting for two weeks. The standard electrolyte turns yellow, whereas the ADP-containing electrolyte remains relatively clear, suggesting improved electrolyte storage stability.

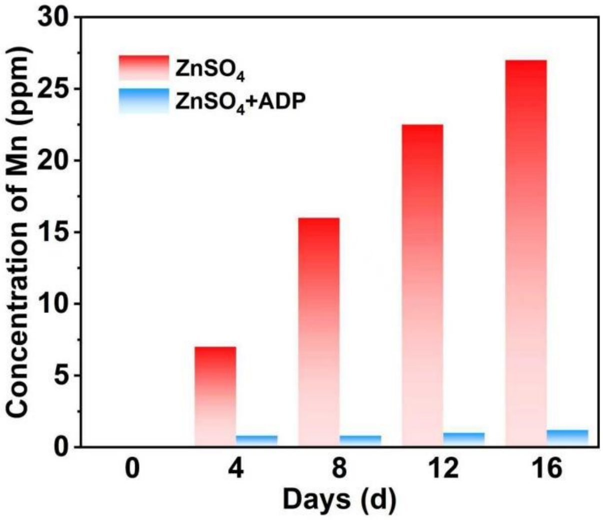

Fig. S31 Quantitative analysis of manganese by inductively coupled plasma optical emission spectrometry (ICP-OES).

1. J. P. Perdew, K. Burke, M. Ernzerhof, *Physical Review Letters*, 1996, **77**, 3865-3868.
2. S. Mukherjee, L. Kavalsky, C. V. Singh, *ACS Applied Materials&Interface*, 2018, **10**, 8630.
3. a) D. V. D. Spoel, E. Lindahl, B. Hess, G. Groenhof, A. E. Mark, H. J. C. Berendsen, *Journal of Computational Chemistry,* 2005, **26,** 1701-1718; b) M. J. Abraham, T. Murtola, R. Schulz, S. Páll, J. C. Smith, B. Hess, E. Lindahl, *SoftwareX*, 2015, **1**, 19-25; c) H. J. C. Berendsen, D. van der Spoel, R. van Drunen, *Computer Physics Communications*, 1995, **91**, 43-56.
4. M. Frisch, G. Trucks, H. Schlegel, G. Scuseria, M. Robb, J. Cheeseman, G. Scalmani, V. Barone, G. Petersson, H. Nakatsuji, *Gaussian Inc. Wallingford CT* 2016, **1**, 572.
5. L. Martínez, R. Andrade, E. G. Birgin, J. M. Martínez, *Journal of Computational Chemistry*, 2009, **30**, 2157-2164.
6. J. Wang, R. M. Wolf, J. W. Caldwell, P. A. Kollman, D. A. Case, *Journal of Computational Chemistry*, 2004, **25**, 1157-1174.
7. A. K. Rappe, C. J. Casewit, K. S. Colwell, W. A. Goddard, III, W. M. Skiff, *Journal of the American Chemical Society,* 1992, **114**, 10024-10035.

8. T. Lu, F. Chen, *Journal of Computational Chemistry,* 2012, **33**, 580-592.

9. A. J. Bard, L. R. Faulkner, "*Electrochemical Methods: Fundamentals and Applications*" John Wiley & Sons 2001.